Molecular Myelin Dysfunction in the Most Common Inherited Peripheral Neuropathies – CMT1A and HNPP

Kathryn R. Moss[1,2,3,*], Dave Gutierrez[1], Ruifa Mi[1], Aysel Cetinkaya-Fisgin[1], Ahmet Höke[1,4]

[1]Department of Neurology, Neuromuscular Division; Johns Hopkins University School of Medicine; Baltimore, MD, 21205; USA

[2]NextGen Precision Health; University of Missouri; Columbia, MO, 65211; USA

[3]Department of Physical Medicine and Rehabilitation, University of Missouri School of Medicine; Columbia, MO, 65211; USA

[4]Department of Neuroscience; Johns Hopkins University School of Medicine; Baltimore, MD, 21205; USA

*Corresponding Author and Lead Contact:

Kathryn R. Moss, PhD
University of Missouri
1030 Hitt Street
Columbia, MO 65211
Tel: 573-882-9412
Email: kmoss@missouri.edu

Abstract

Increased and decreased dosage of the *Peripheral Myelin Protein 22* (*PMP22*) gene cause dysmyelinating peripheral neuropathy. Charcot-Marie-Tooth Disease Type 1A (CMT1A, *PMP22* duplication) and Hereditary Neuropathy with Liability to Pressure Palsies (HNPP, *PMP22* deletion) are the most common inherited peripheral neuropathies, yet gaps remain about their pathophysiology and pathomechanims. Our previous results with CMT1A model mice demonstrate that muscle atrophy occurs without evidence of secondary axon degeneration suggesting that primary myelin dysfunction may contribute to functional deficits in CMT1A and motivating investigation of myelin dysfunction. Here we used CMT1A and HNPP model mice and confocal immunofluorescence imaging of teased tibial nerve fibers to determine how altered PMP22 expression disrupts myelin integrity and reveal CMT1A and HNPP pathomechanisms. We identified dramatic changes to molecular machinery at Schmidt-Lanterman incisures (SLIs) and Nodes of Ranvier that led us to propose two potential pathomechanisms for CMT1A and HNPP: impaired metabolic support and axonal ion disequilibrium. We also developed a working model for these pathomechanims that is driven by PMP22-mediated regulation of adherens junctions. Ongoing studies are aimed at testing these proposed pathomechanisms and determining how altered PMP22 and adherens junctions cause these defects. This work will provide insight into CMT1A and HNPP pathogenesis and may reveal novel approaches for developing therapeutics.

Introduction

Charcot-Marie-Tooth Disease Type 1A (CMT1A) and Hereditary Neuropathy with Liability to Pressure Palsies (HNPP) are the most common inherited peripheral neuropathies. The prevalence of all types of CMT is 1:2,500 and CMT1A and HNPP account for ~65% of genetically defined CMT cases[1]. Remarkably, these diseases are caused by copy number variation of the same gene; CMT1A is caused by duplication of the *Peripheral Myelin Protein 22* (*PMP22*) gene and HNPP is caused by deletion of the *PMP22* gene. CMT1A and HNPP patients present with similar symptoms but vary with regard to age of onset, progression and severity. CMT1A patients experience a progressive dysmyelinating peripheral neuropathy with more severe sensory and motor deficits usually beginning during childhood[2]. HNPP patients experience an acute sensory and motor dysmyelinating peripheral neuropathy due to repeated focal pressure and although recovery is common, permanent injury can result from repeated compression events[3]. HNPP symptoms generally begin during adolescence or early adulthood, but HNPP is thought to be underdiagnosed and is often misdiagnosed[3]. Although both diseases dramatically impact patient quality of life and burden the healthcare system, there are currently no disease-modifying treatments available.

PMP22 is a Schwann cell-enriched gene and even though CMT1A and HNPP pathogenesis initially occurs in myelinating Schwann cells, secondary axon degeneration as a consequence of myelin dysfunction has been suggested to drive functional deficits in patients[4,5]. However, our previous results with CMT1A model mice revealed negligible evidence of denervation and secondary axon degeneration despite their strong neuromuscular behavioral deficits, dramatically reduced tibial nerve CMAP amplitudes (~50%) and muscle atrophy as determined by gastrocnemius muscle fiber cross sectional area and total muscle mass[6]. These findings indicated that primary myelin dysfunction may play a critical role in driving CMT1A pathogenesis and provided rationale for investigating mechanisms of myelin dysfunction in CMT1A and HNPP model mice. This inquiry was guided by previous reports regarding the physiological function of PMP22.

PMP22 is a member of the Claudin superfamily of proteins (pfam00822), and current evidence suggests that PMP22 plays an undefined role in cell adhesion[7]. Orthodox claudins establish selective barriers as components of tight junction complexes and although PMP22 is a distant cousin (i.e., 25% sequence identity

and 41% sequence similarity as compared to Claudin-1), the protein topology is homologous and the structural similarity between their extracellular loops is striking (AlphaFold predicted structures). PMP22 is enriched in myelinating Schwann cells where it localizes to compact myelin[8], but it is also expressed in other cell types. PMP22 co-localizes with tight junction components (ZO-1 and Occludin) at cell boarders in epithelial and endothelial cells and PMP22 overexpression results in increased transepithelial electrical resistance in epithelial cells[9-11]. PMP22 also affects adhesion junction components in peripheral nerve myelin. The distribution of tight junction (Claudin-19, ZO-1, ZO-2 and JAM-C) and adherens junction (E-Cadherin) components is disturbed in heterozygous (HNPP model) and homozygous PMP22 knockout mice[12-14]. Therefore, it seems likely that PMP22 functions similarly to Claudin proteins and regulates the organization of adhesion complexes in myelin.

Here we used CMT1A and HNPP model mice and confocal immunofluorescence imaging of teased tibial nerve fibers to determine how altered PMP22 expression disrupts myelin integrity and reveal CMT1A and HNPP pathomechanisms. We identified dramatically disorganized adherens junctions at Schmidt-Lanterman incisures (SLIs) in CMT1A and HNPP model myelin which mimicked the effect of the SLI marker F-Actin indicating that the overall morphology of SLIs is compromised. SLIs and adherens junctions were more compact in CMT1A and more spread out in HNPP. The SLI component Connexin29 was also disorganized in CMT1A and HNPP model myelin, but the effect did not conform to the previous trend. Connexin29 was more spread out with focal accumulations often visible outside of SLIs in CMT1A and this effect was the same but less dramatic in HNPP. Preliminary results with CMT1A model myelin indicate that the SLI component MAG was also much more diffuse. The interconnectedness of SLIs and Nodes of Ranvier through the inner mesaxon and previous reports demonstrating that Connexin29 also associates with Kv1 channels at juxtaparanodes led us to evaluate Node of Ranvier organization. Our preliminary findings reveal Kv1.2 patterning defects and potentially nodal widening of Nav channels. Paranodal junctions were also assessed and Caspr1 distribution was disturbed similar to Kv1.2. The Kv1.2 and Caspr defects appeared more dramatic in CMT1A as compared to HNPP. These results led us to propose two potentially cooperative pathomechanisms for CMT1A and HNPP: impaired metabolic support and axonal ion disequilibrium. Both mechanisms could affect nerve conduction properties and contribute to functional decline. Ongoing studies are aimed at testing these proposed

pathomechanisms and determining how altered PMP22 and adherens junctions cause these defects. This work will provide insight into CMT1A and HNPP pathogenesis and may reveal novel approaches for developing therapeutics.

Results

Adherens Junction Defects at SLIs in Peripheral Nerve Myelin from CMT1A and HNPP Model Mice

Constitutive mouse models of CMT1A (C3-PMP)[15] and HNPP (LacZ PMP22 deficient)[16] were utilized to evaluate adhesion junctions in peripheral nerve myelin. Teased nerve fibers were prepared from the tibial branch of the sciatic nerve and processed for confocal immunofluorescence imaging. CMT1A fibers were initially stained for markers of tight junctions (ZO-1) and adherens junctions (E-Cadherin). ZO-1 was primarily localized to the paranode and did not exhibit altered expression or localization in CMT1A (data not shown). However, E-Cadherin, which is localized to SLIs, paranodes and inner mesaxons, was severely disturbed in CMT1A. The signal is more punctate and the funnel shape structure of SLIs is often disrupted (Figure 1A). E-Cadherin mean and distribution (volume of thresholded signal normalized to fiber diameter) were quantified at SLIs. The data were analyzed by unpaired t-test on all SLIs (n=5, ~30 SLIs/n) and the average from each biological replicate (n=5). E-Cadherin mean trended towards an increase (significant only with statistics on all SLIs) which is likely not biologically significant, but E-Cadherin distribution at SLIs was significantly reduced by both statistical measures (Figures 1B-C). The distribution of E-Cadherin at SLIs in teased nerve fibers from HNPP model mice appeared to demonstrate the opposite effect as compared to CMT1A, more spread out (Figure 1D). However, quantification revealed that the mean and distribution of E-Cadherin at SLIs in HNPP was unchanged as compared to wildtype (Figures 1E-F), but these datasets are incomplete (n=3, ~30 SLIs/n).

The core complex of adherens junctions consists of the single pass transmembrane protein E-cadherin and three cytoplasmic catenin proteins (p120-Catenin, β-Catenin and α-Catenin) which connect the cadherin complex to the actin cytoskeleton and multiple signaling pathways[17]. β-Catenin and p120-Catenin were also assessed by confocal immunofluorescence imaging to grossly evaluate adherens junction complex assembly. β-Catenin clearly remained co-localized with E-Cadherin in CMT1A and HNPP model myelin (Figure 2A, D). Quantification indicated that mean β-Catenin at SLIs was unchanged in CMT1A (n=5, ~30 SLIs/n, Figure 2B) and increased at SLIs in HNPP but potentially biologically insignificantly (n=3, ~30 SLIs/n, Figure 2E). β-Catenin distribution at SLIs mimicked the effects observed with E-Cadherin; reduced in CMT1A (n=5, ~30 SLIs/n, Figure 2C) and likely increased in HNPP (n=3, ~30 SLIs/n, Figure 2F). p120-Catenin also remained co-

localized with E-Cadherin in CMT1A and HNPP (Figures 3A, D) but quantification of p120-Catenin mean and distribution at SLIs was much more variable. As such, p120-Catenin mean at SLIs was unchanged in CMT1A (n=4, ~30 SLIs/n, Figure 3B) and HNPP (n=3, ~30 SLIs/n, Figure 3E) and p120-Catenin distribution at SLIs was unchanged in CMT1A (n=4, ~30 SLIs/n, Figure 3C). The only significant measure was p120-Catenin distribution at SLIs in HNPP, which was increased but likely has not yet reached biological significance (n=3, ~30 SLIs/n, Figure 3F).

The variability in the distribution of p120-Catenin at SLIs was further explored by plotting p120-Catenin distribution against E-Cadherin distribution at each individual SLI (n=2, ~30 SLIs/n). The values are strongly positively correlated in both CMT1A and wildtype myelin which was expected given that these proteins are known to form a complex (Figure 4). However, a population of SLIs with large volumes of p120-Catenin and E-Cadherin became apparent indicating that the distribution of p120-Catenin may predict the distribution of E-Cadherin. These high-volume escapers likely account for some of the variability in the Figure 3 data and suggest that p120-Catenin may counteract the drive towards reduced E-Cadherin distribution at SLIs in CMT1A. This is consistent with the known role for p120-Catenin in regulating E-Cadherin stability[18].

SLI Gross Morphology in Peripheral Nerve Myelin from CMT1A and HNPP Model Mice

Adherens junctions function to stabilize cell-cell interactions and maintain the structural integrity of cells and cellular compartments[19]. Given the dramatic changes in adherens junctions at SLIs in CMT1A and HNPP, gross SLI morphology was also evaluated by labeling F-Actin with Phalloidin (representative images in Figures 1A, D). F-Actin is often used as a marker for SLIs given that all cytoplasmic-like compartments in myelin are actin-rich. Mean F-Actin was unchanged at SLIs in CMT1A, but the distribution of F-Actin was extremely reduced (n=5, ~30 SLIs/n, Figures 5A-B). Conversely, mean F-Actin was increased at SLIs in HNPP consistent with a pervious report[20], although yet to reach biological significance (n=3, ~30 SLIs/n, Figure 5C). And the distribution of F-Actin at SLIs in HNPP was extremely increased (n=3, ~30 SLIs/n, Figure 5D). These results indicate that gross SLI morphology is altered in myelin from CMT1A and HNPP model mice: compacted in CMT1A and broadened in HNPP.

SLI - Inner Mesaxon - Node of Ranvier Continuum Defects in Peripheral Nerve Myelin from CMT1A and HNPP Model Mice

Additional SLI components were assessed to determine if they mimicked the effects observed with adherens junctions and F-Actin. Connexin29 (Cx29), a gap junction family protein, and Myelin Associated Glycoprotein (MAG), an immunoglobulin superfamily protein, were also evaluated by confocal immunofluorescence imaging. The SLI compartment visible with Cx29 and MAG staining is discrete in wildtype myelin but appears fuzzy and diffuse in HNPP and especially in CMT1A (Figures 6A, D). Cx29 mean and distribution at SLIs were dramatically increased in CMT1A (n=5, ~30 SLIs/n, Figure 6B-C). Preliminary results demonstrate that mean Cx29 is likely also increased in HNPP but less dramatically than in CMT1A (n=1, ~30 SLIs/n, Figure 6F). Mean MAG is also likely dramatically increased at SLIs but has yet to reach biological significance (n=3, ~30 SLIs/n) and distribution analysis has yet to be performed. The increased distribution of Cx29 and MAG at SLIs in CMT1A and likely HNPP is accompanied by focal accumulations of these proteins outside of SLI compartments supporting the notion that SLI integrity is compromised. Cx29 and MAG are not only localized to SLIs but also to the inner mesaxon and juxtparanode[21-23], highlighting the interconnectedness of SLIs and the nodal region through the inner mesaxon. Cx29 is suggested to co-localize with Kv1 channels at juxtaparanodes to electrically couple axons to myelinating Schwann cells allowing for rapid repolarization and fast conduction velocities in mammals[23]. Additionally, MAG deficient mice develop paranode defects[24]. This prompted the characterization of Nodes of Ranvier in CMT1A and HNPP model mice.

Node of Ranvier Patterning Defects in Peripheral Nerve Myelin from CMT1A and HNPP Model Mice

Nodes of Ranvier are spatially organized into three distinct regions, the node, paranode and juxtaparanode, to allow for saltatory conduction of action potentials along axons. The node contains voltage-gated sodium channels for depolarization, the juxtaparanode contains voltage-gated potassium channels for repolarization and the paranode contains septate-like junctions to separate the node and juxtaparanode domains[25]. Kv1.1 and Kv1.2 are the primary voltage-gated potassium channels in fast-conduction peripheral

nerve axons[21]. Nodes and juxtaparanodes were first assessed in CMT1A and HNPP teased nerved fibers by staining with pan-Nav and anti-Kv1.2 antibodies, respectively. Our preliminary results indicate that voltage-gated sodium channels at nodes may be more diffuse indicating nodal widening and that Kv1.2 organization is dramatically disrupted (Figure 7). The enrichment of Kv1.2 at juxtaparanodes is frequently diminished and Kv1.2 is spread along the internode with a patchy distribution (Figure 7). This trend holds true for both CMT1A and HNPP but quantification is ongoing to determine whether these defects are more severe in CMT1A and compared to HNPP as predicted on initial assessment. Given the role of paranodal septate-like junctions in organizing Nodes of Ranvier, members of this protein complex, Neurofascin155 (NF155) and Caspr1 were also evaluated by confocal immunofluorescence imaging. The anti-NF155 is likely not specific for only NF155 given that it is localized to nodes and paranodes. However, it does not appear dramatically altered in CMT1A or HNPP (Figure 8). Caspr1 is severely altered though; the compact Caspr1 plaque at paranodes is fragmented and inner mesaxons appear much more spiraled (Figure 8). Again, this trend holds true for both CMT1A and HNPP with CMT1A demonstrating more dramatic defects, but quantification is ongoing.

Phenotype to Pathomechanism for CMT1A and HNPP - Impaired Metabolic Support & Axonal Ion Disequilibrium

It is probable that the severe changes in SLI and Node of Ranvier molecular organization and likely morphology contribute to CMT1A and HNPP pathogenesis. Our results led us to propose two potential pathomechanisms for CMT1A and HNPP that could be working in tandem: impaired metabolic support and axonal ion disequilibrium. In support of altered metabolism, the density of SLIs was assessed given that large caliber myelinated fibers have been demonstrated to contain a higher density of SLIs likely due to their increased metabolic demands. SLI density was quantified by measuring the distance between SLIs which were labeled with anti-β-Catenin and/or Phalloidin (Figure 9A). Preliminary results with CMT1A teased nerve fibers indicate that the average distance between SLIs is dramatically reduced indicating a higher SLI density (n=2, ~60 myelin sheaths/n, Figure 9B). Given that peripheral nerves from CMT1A model mice exhibit a loss of large caliber myelinating axon fibers, the distance between SLIs was plotted against nerve fiber diameter to determine

how fiber diameter affects SLI density. The wildtype data demonstrate a negative correlation supporting the notion that larger caliber myelinated axons contain a higher density of SLIs (Figure 9C). However, SLI density was consistent across fiber diameters in CMT1A indicating that all CMT1A myelinated axons may have a higher metabolic need regardless of their caliber (Figure 9C). Additional experiments to test the proposed pathomechanims of impaired metabolic support and axonal ion disequilibrium in CMT1A and HNPP model mice are ongoing.

Discussion

The lack of evidence for secondary axon degeneration in rodent models of CMT1A has motivated investigation into mechanisms of primary myelin dysfunction in CMT1A and HNPP model mice. This study was guided by previous reports describing a role of PMP22 in adhesion. Kv1.1 and E-Cadherin were qualitatively reported to have an altered distribution in teased sciatic and femoral nerves from PMP22 homozygous knockout mice which became more severe at 9-weeks of age as compared to 3-weeks of age[12]. Additionally, E-Cadherin and MAG were demonstrated to be altered in paraffin sections of sciatic nerves from PMP22 heterozygous knockout mice as quantified qualitatively by percent abnormal SLIs and paranodes[20]. E-Cadherin was affected earlier at 1-month of age and onward as compared to 5-months of age and onward for MAG [20]. Mean F-Actin labeled by Rhodamine Phalloidin was also reported to be increased at SLIs and paranodes in teased sciatic nerves starting at 3-months of age but Caspr1 and NF155 were suggested to be normal at paranodes[20]. It should also be noted that this model of HNPP is different from the LacZ PMP22 Deficient mice.

This study sought to build upon these findings and determine how excess PMP22 expression in CMT1A affects adhesion complexes. Using constitutive CMT1A and HNPP mouse models and quantitative confocal immunofluorescence imaging, we revealed that multiple adherens junction components are dramatically disorganized in teased tibial nerve fibers from CMT1A and HNPP model mice. The spatial organization of E-Cadherin and β-Catenin is compacted at SLIs in CMT1A and broadened at SLIs in HNPP. The mean and distribution of p120-Catenin are more variable at SLIs in CMT1A and HNPP, but increased p120-Catenin distribution is likely predictive and potentially causative of improved E-Cadherin distribution at SLIs in CMT1A. The distribution of F-Actin at SLIs mimicked the effects observed with E-Cadherin and β-Catenin but was even more severe indicating the gross SLI morphology is likely disturbed. Mean F-Actin was also increased at SLIs in HNPP substantiating the published results described previously[20]. The SLI components Cx29 and MAG were also affected at SLIs in CMT1A and HNPP model myelin but in a distinct manner. Mean Cx29 was increased at SLIs in both CMT1A and HNPP but to a higher degree in CMT1A. The distribution of Cx29 was also dramatically increased at SLIs in CMT1A but Cx29 SLI distribution has yet to be quantified in

HNPP. Mean Additionally, mean MAG was increased at SLIs in CMT1A but CMT1A distribution and HNPP fibers have yet to be quantified. The localization of Cx29 and MAG to inner mesaxons and juxtaparanodes and the co-localization of Cx29 with Kv1 channels at juxtaparanodes prompted us to characterize Nodes of Ranvier. Preliminary results indicate that Kv1.2 is less enriched at juxtaparanodes with focal accumulations frequently spread along the internode. Nav at nodes is also likely broadened indicating nodal widening. The pranodal septate-like junction component Caspr1 is also disturbed; the compact plaque at paranodes is often segmented and inner mesaxons are more spiraled. The Node of Ranvier defects appear more dramatic in CMT1A as compared to HNPP, but quantification is ongoing.

These results led us to propose two pathomechanisms for CMT1A and HNPP that may be working in concert: impaired metabolic support and axonal ion disequilibrium. Both mechanisms could affect nerve conduction and contribute to CMT1A and HNPP pathogenesis. Preliminary support for impaired metabolism in CMT1A model myelin is evidenced by an increased density of SLIs which is not dependent upon nerve fiber diameter. Ongoing studies are testing these proposed pathomechanisms. Understanding mechanisms that drive CMT1A and HNPP pathogenesis will provide critical insight for designing efficacious therapies. This objective is hindered by key gaps that remain regarding the physiological function of PMP22 in myelin. Our results support a function for PMP22 in adhesion and taken together with reports providing evidence that PMP22 and E-Cadherin interact in myelin[13] and that adherens junctions are required for proper myelin architecture, particularly SLIs and paranodes,[14,26] led us to propose the following working model. PMP22 regulates adherens junctions which control peripheral nerve myelin architecture. And altered cellular and molecular peripheral nerve myelin architecture in CMT1A and HNPP due to abnormal adherens junctions causes impaired metabolic support and axonal ion disequilibrium contributing to CMT1A and HNPP pathogenesis. This model and consequent pathomechanisms would suggest that primary myelin dysfunction may be integral in driving CMT1A and HNPP functional decline and challenges the current paradigm that secondary axon degeneration is primarily responsible. We anticipate the results from these inquiries to identify novel therapeutic approaches for CMT1A, HNPP and potentially other dymyelinating peripheral neuropathies.

Figures and Legends

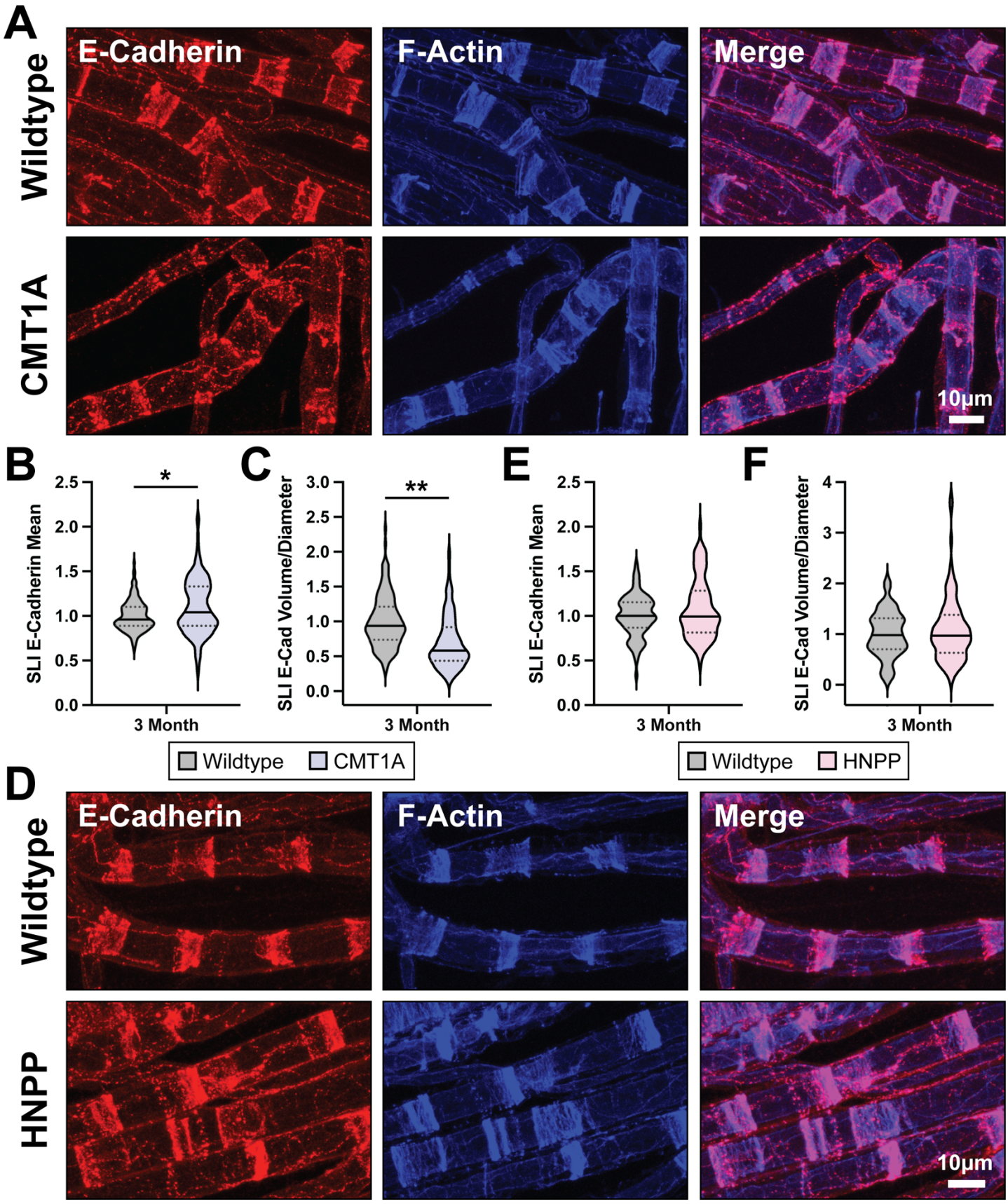

Figure 1. Dramatic E-Cadherin Defects at SLIs in Peripheral Nerve Myelin from CMT1A and HNPP

Model Mice. Representative images of 3-month-old **(A)** wildtype (WT, C57BL/6J) and CMT1A or **(D)** WT (129S1/SvImJ) and HNPP teased tibial nerve fibers stained for the adherens junction protein E-Cadherin (red, at SLIs and inner mesaxons) and F-Actin (blue). Quantification of the following at SLIs: **(B)** E-Cadherin mean in CMT1A, **(C)** E-Cadherin distribution (E-Cadherin signal volume/fiber diameter) in CMT1A, **(E)** E-Cadherin mean in HNPP and **(F)** E-Cadherin distribution in HNPP. CMT1A n=5 animals, HNPP n=3 animals (~30 SLIs/animal). Violin plots (solid black line: median, dashed black lines: quartiles), unpaired t-test, *$p < 0.05$ (individual), **$p < 0.05$ (average). Scale bars, 10µm.

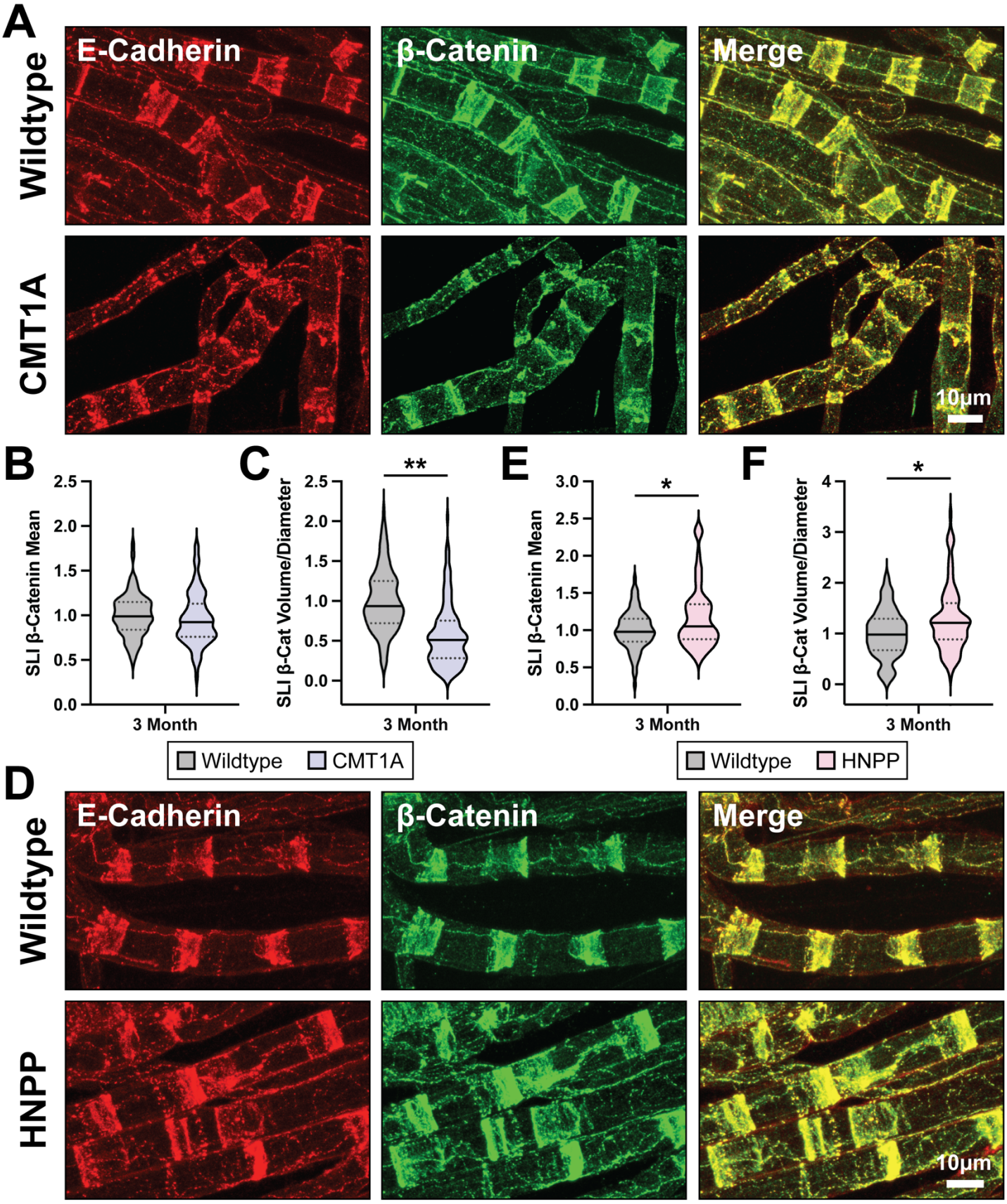

Figure 2. Dramatic β-Catenin Defects at SLIs in Peripheral Nerve Myelin from CMT1A and HNPP Model Mice. Representative images of 3-month-old **(A)** WT (C57BL/6J) and CMT1A or **(D)** WT

(129S1/SvImJ) and HNPP teased tibial nerve fibers stained for the adherens junction complex proteins β-Catenin (green) and E-Cadherin (red). Quantification of the following at SLIs: **(B)** β-Catenin mean in CMT1A, **(C)** β-Catenin distribution in CMT1A, **(E)** β-Catenin mean in HNPP and **(F)** β-Catenin distribution in HNPP. CMT1A n=5 animals, HNPP n=3 animals (~30 SLIs/animal). Violin plots (solid black line: median, dashed black lines: quartiles), unpaired t-test, *$p < 0.05$ (individual), **$p < 0.05$ (average). Scale bars, 10μm.

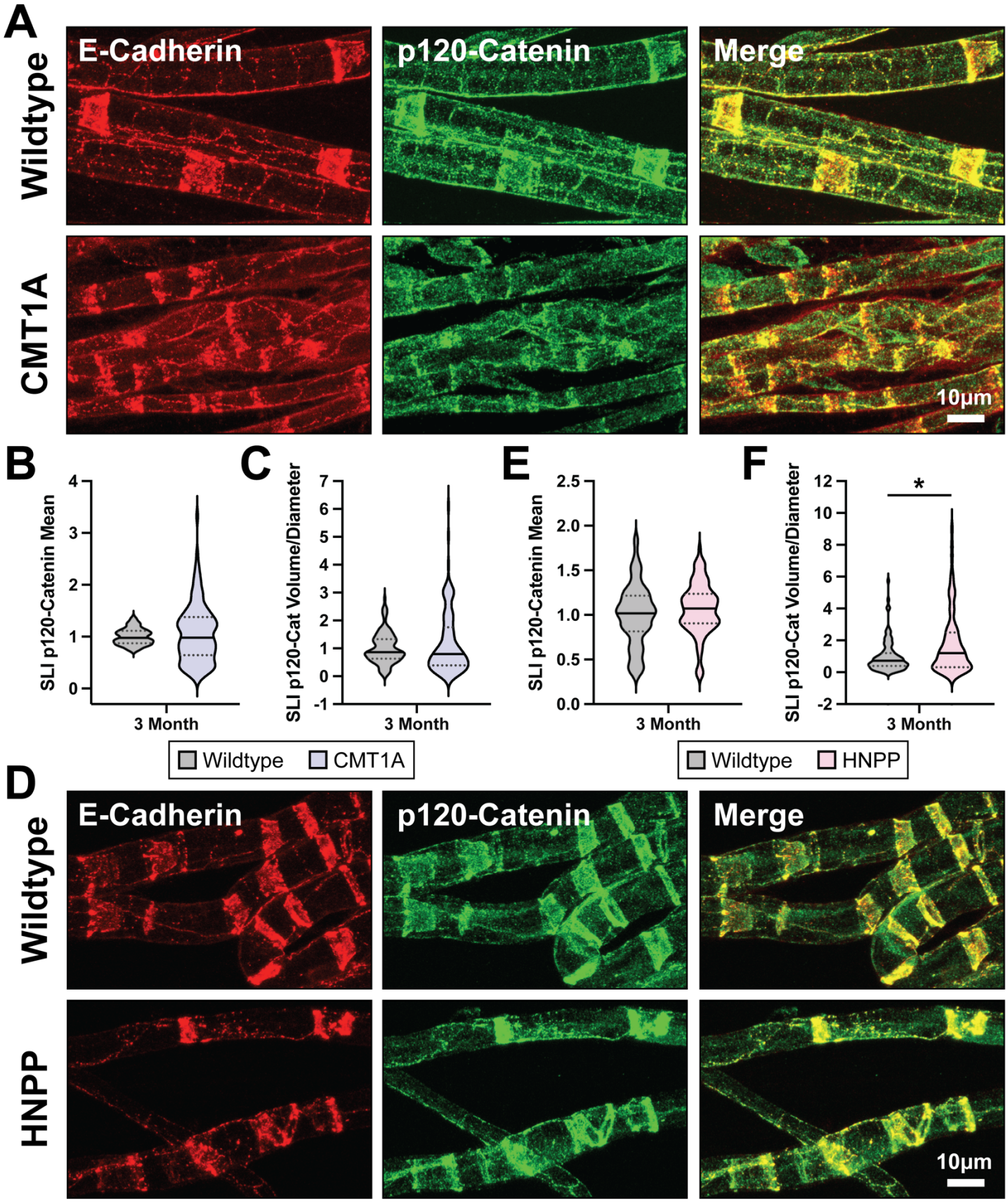

Figure 3. Variable p120-Catenin Defects at SLIs in Peripheral Nerve Myelin from CMT1A and HNPP Model Mice. Representative images of 3-month-old **(A)** WT (C57BL/6J) and CMT1A or **(D)** WT

(129S1/SvImJ) and HNPP teased tibial nerve fibers stained for the adherens junction complex proteins p120-Catenin (green) and E-Cadherin (red). Quantification of the following at SLIs: **(B)** p120-Catenin mean in CMT1A, **(C)** p120-Catenin distribution in CMT1A, **(E)** p120-Catenin mean in HNPP and **(F)** p120-Catenin distribution in HNPP. CMT1A n=4 animals, HNPP n=3 animals (~30 SLIs/animal). Violin plots (solid black line: median, dashed black lines: quartiles), unpaired t-test, *$p < 0.05$ (individual). Scale bars, 10µm.

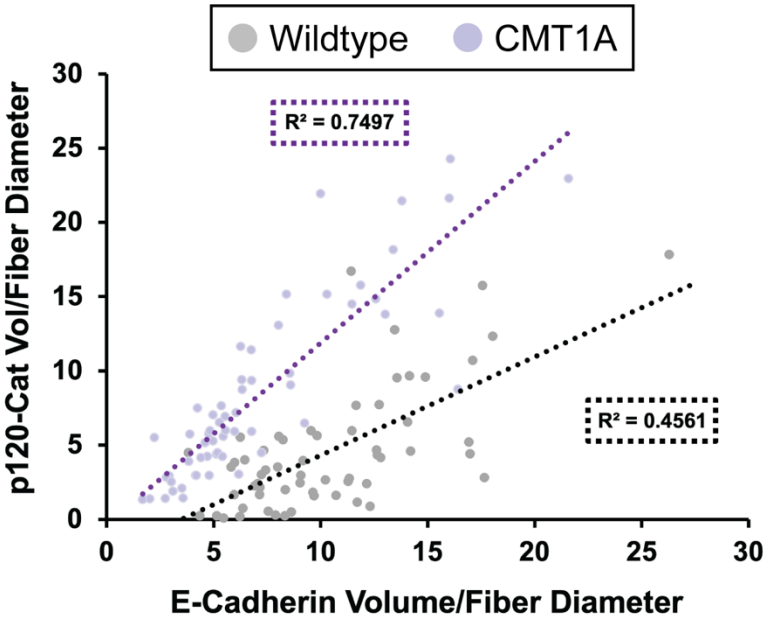

Figure 4. Positive Correlation Between p120-Catenin Distribution and E-Cadherin Distribution at SLIs in Peripheral Nerve Myelin from CMT1A Model Mice. Scatter plot of p120-Catenin distribution against E-Cadherin distribution at individual SLIs (n=2 animals, ~30 fibers/mouse). R^2 values for the trendlines are outlined in matching colors.

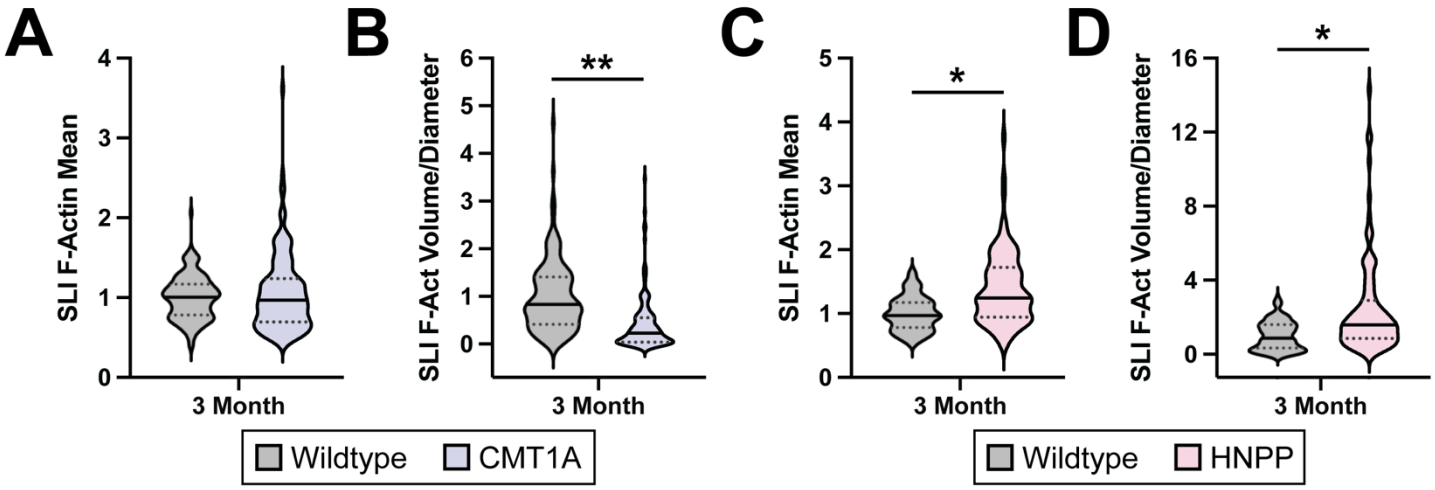

Figure 5. F-Actin Defects Consistent with Adherens Junction Changes at SLIs in Peripheral Nerve Myelin from CMT1A and HNPP Model Mice. Representative images of 3-month-old WT/CMT1A and WT/HNPP teased tibial nerve fibers stained for F-Actin with Phalloidin are shown in Figure 1. Quantification of the following at SLIs: **(A)** F-Actin mean in CMT1A, **(B)** F-Actin distribution in CMT1A, **(C)** F-Actin mean in HNPP and **(D)** F-Actin distribution in HNPP. CMT1A n=5 animals, HNPP n=3 animals (~30 SLIs/animal). Violin plots (solid black line: median, dashed black lines: quartiles), unpaired t-test, *$p < 0.05$ (individual), **$p < 0.05$ (average).

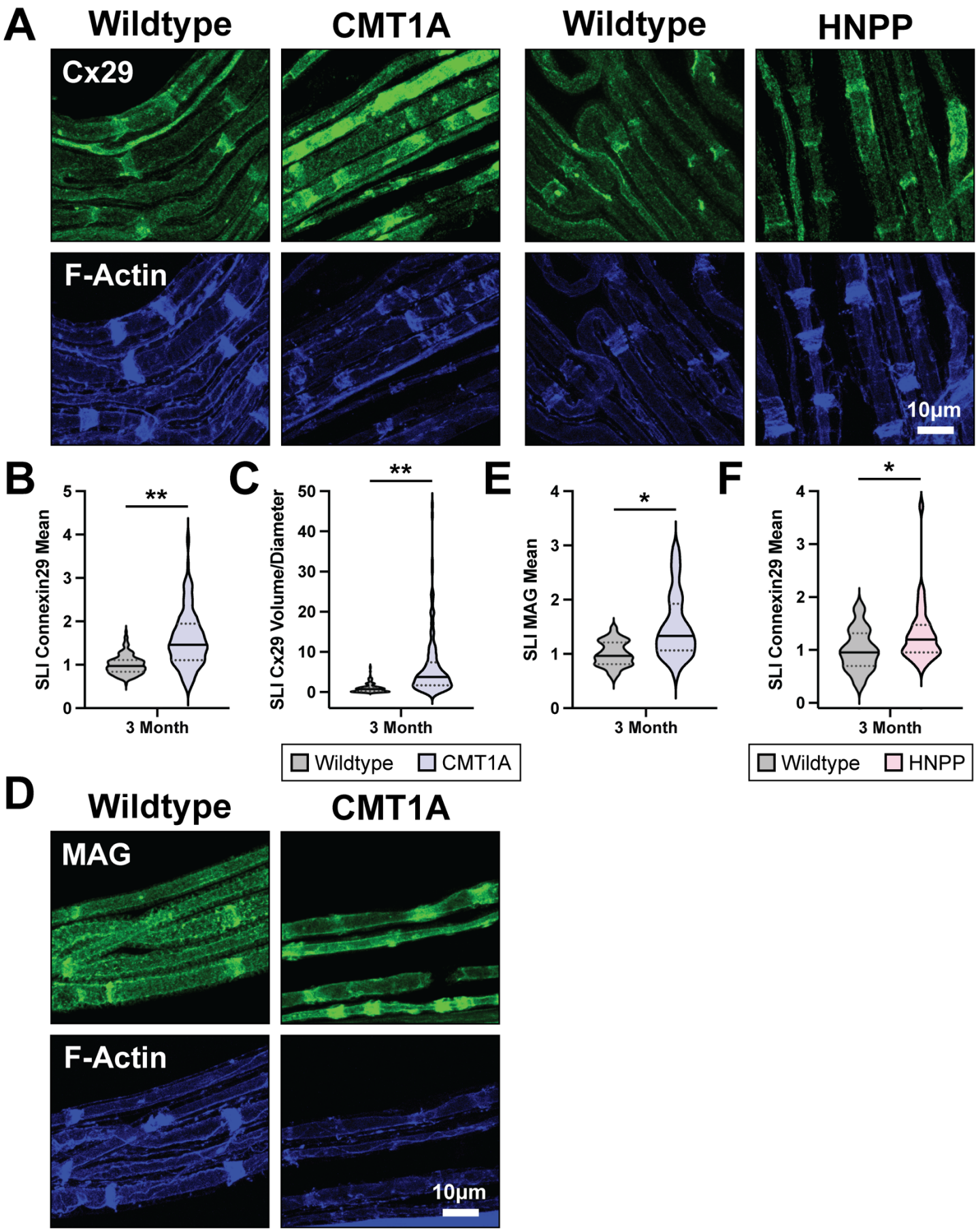

Figure 6. Dramatic but Distinct Connexin29 and MAG Defects at SLIs in Peripheral Nerve Myelin from

CMT1A and HNPP Model Mice. (A) Representative images of 3-month-old WT (C57BL/6J) and CMT1A or WT (129S1/SvImJ) and HNPP teased tibial nerve fibers stained for Connexin29 (Cx29, green) and F-Actin (blue). Quantification of the following at SLIs: **(B)** Connexin29 mean in CMT1A, **(C)** Connexin29 distribution in CMT1A, **(F)** Connexin29 mean in HNPP. **(D)** Representative images of 3-month-old WT (C57BL/6J) and CMT1A teased tibial nerve fibers stained for MAG (green) and F-Actin (blue). **(E)** Quantification of MAG mean in CMT1A. Connexin29: CMT1A n=5 animals, HNPP n=1 animal; MAG: CMT1A n=3 animals (~30 SLIs/animal). Violin plots (solid black line: median, dashed black lines: quartiles), unpaired t-test, *$p < 0.05$ (individual), **$p < 0.05$ (average). Scale bars, 10µm.

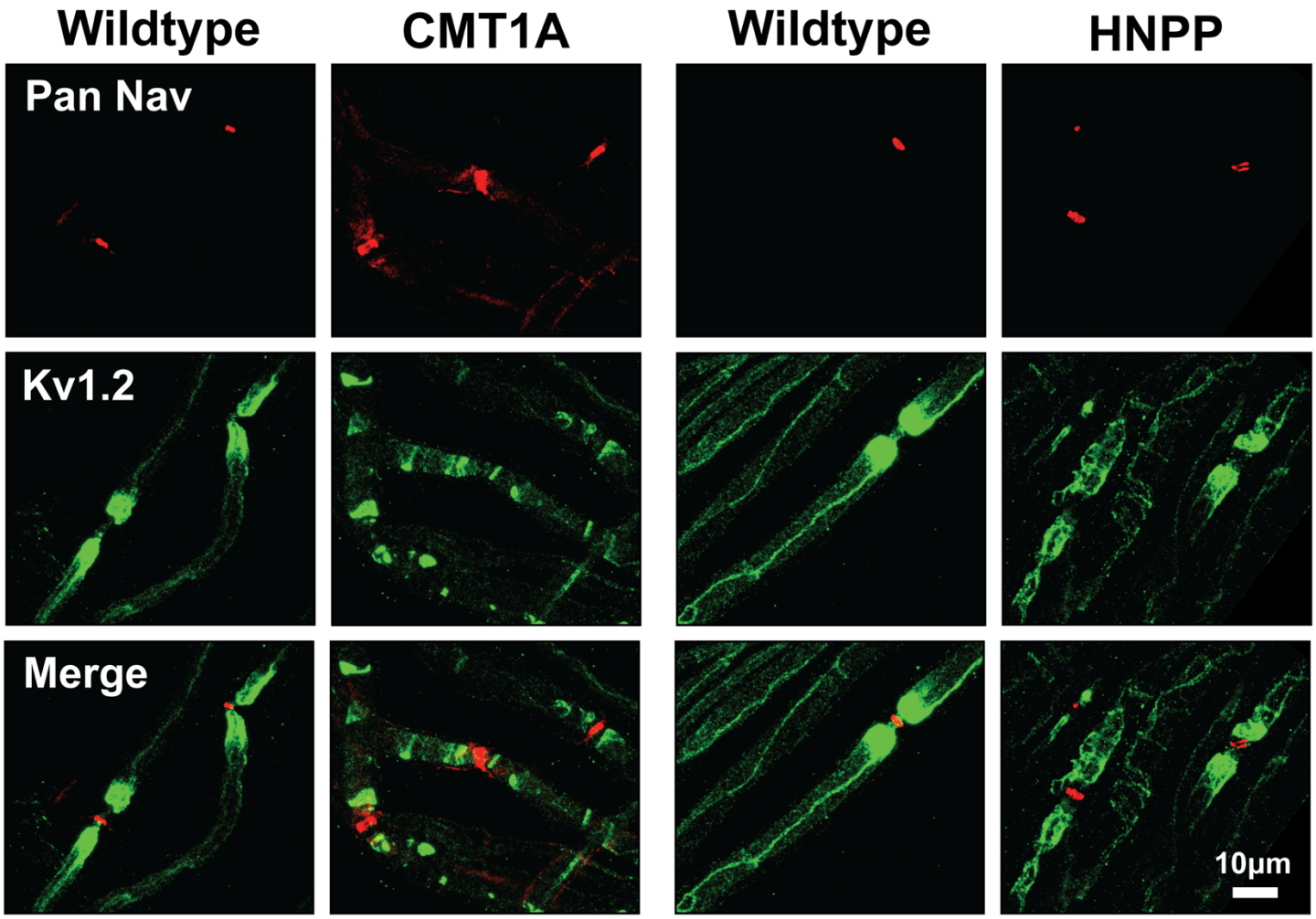

Figure 7. Kv1.2 at Juxtaparanodes and Nav at Nodes Preliminarily Demonstrate Patterning Defects in

Peripheral Nerve Myelin from CMT1A and HNPP Model Mice. Representative images of 3-month-old WT (C57BL/6J) and CMT1A or WT (129S1/SvImJ) and HNPP teased tibial nerve fibers stained with anti-Pan Nav (red) and anti-Kv1.2 (green). Scale bars, 10µm.

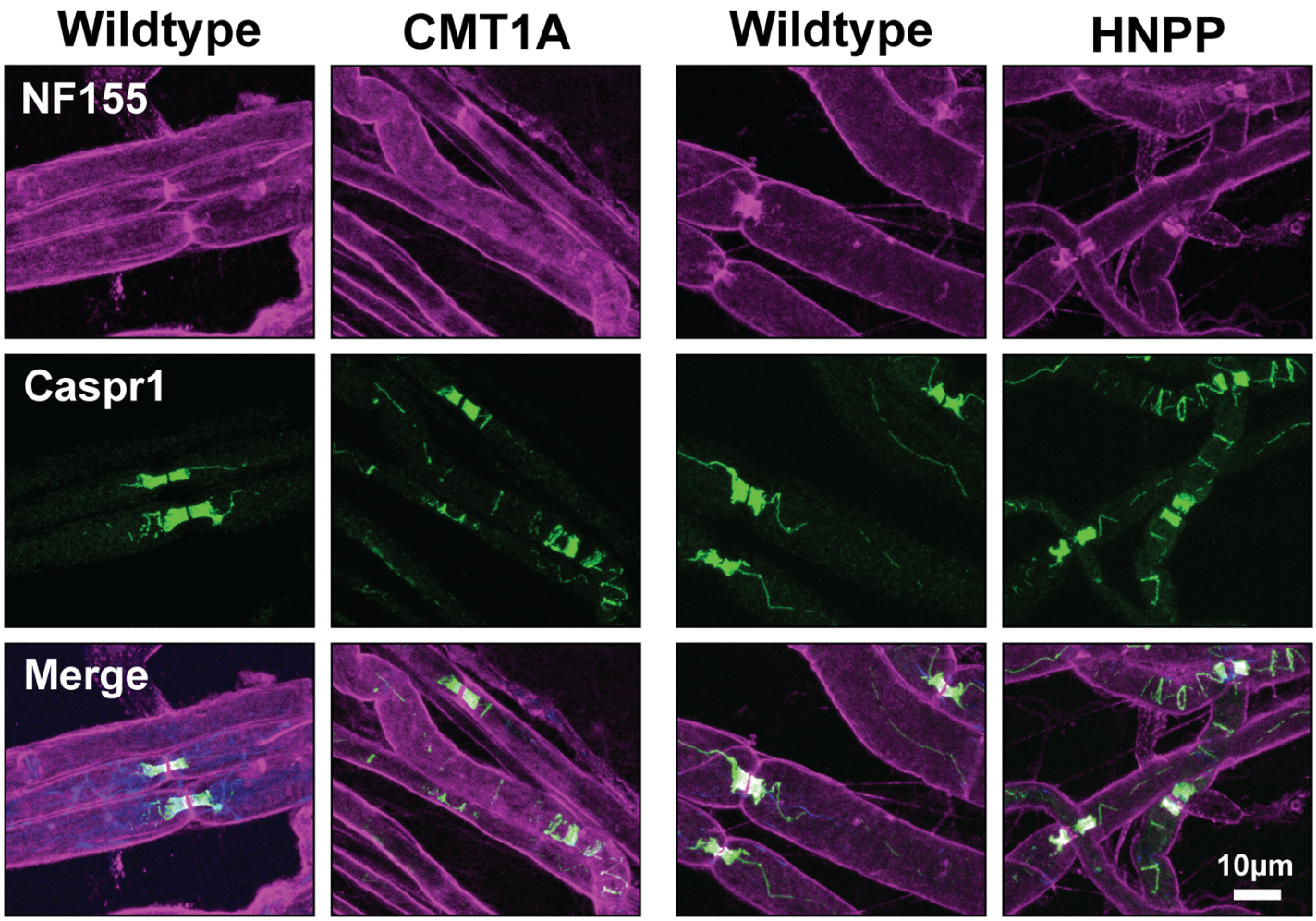

Figure 8. Caspr1 at Paranodes Preliminarily Demonstrates Patterning Defects in Peripheral Nerve Myelin from CMT1A and HNPP Model Mice. Representative images of 3-month-old WT (C57BL/6J) and CMT1A or WT (129S1/SvImJ) and HNPP teased tibial nerve fibers stained for Neurofascin155 (NF155, pink) and Caspr1 (green). Scale bars, 10µm.

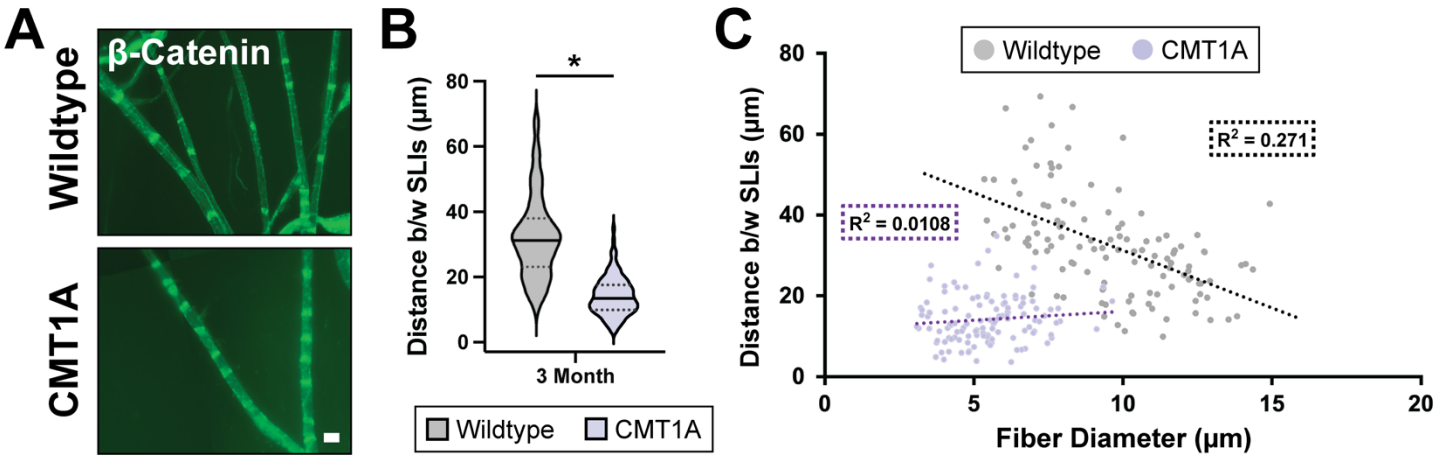

Figure 9. Evidence for Impaired Metabolic Support as a Pathomechanism of Myelin Dysfunction in CMT1A Model Mice. (A) Representative images of 3-month-old WT (C57BL/6J) and CMT1A teased tibial nerve fibers stained for β-Catenin (green) to label SLIs. **(B)** Quantification of average distance between SLIs as determined by measuring the distance between the funnel shape structures and averaging these distances for each myelin sheath. **(C)** Scatter plot of average distance between SLIs against nerve fiber diameter. n=2 animals (~60 fibers/animal). Violin plot (solid black line: median, dashed black lines: quartiles), unpaired t-test, *$p < 0.05$ (individual). Scale bar, 10µm.

References

1. Li, J., Parker, B., Martyn, C., Natarajan, C. & Guo, J. The PMP22 gene and its related diseases. *Mol Neurobiol* **47**, 673-698 (2013).
2. Watila, M.M. & Balarabe, S.A. Molecular and clinical features of inherited neuropathies due to PMP22 duplication. *J Neurol Sci* **355**, 18-24 (2015).
3. Attarian, S., Fatehi, F., Rajabally, Y.A. & Pareyson, D. Hereditary neuropathy with liability to pressure palsies. *J Neurol* **267**, 2198-2206 (2020).
4. Krajewski, K.M.*, et al.* Neurological dysfunction and axonal degeneration in Charcot-Marie-Tooth disease type 1A. *Brain* **123 (Pt 7)**, 1516-1527 (2000).
5. Manganelli, F.*, et al.* Nerve conduction velocity in CMT1A: what else can we tell? *Eur J Neurol* **23**, 1566-1571 (2016).
6. Moss, K.R.*, et al.* SARM1 knockout does not rescue neuromuscular phenotypes in a Charcot-Marie-Tooth disease Type 1A mouse model. *J Peripher Nerv Syst* **27**, 58-66 (2022).
7. Simske, J.S. Claudins reign: The claudin/EMP/PMP22/gamma channel protein family in C. elegans. *Tissue Barriers* **1**, e25502 (2013).
8. Vallat, J.M.*, et al.* Ultrastructural PMP22 expression in inherited demyelinating neuropathies. *Ann Neurol* **39**, 813-817 (1996).
9. Notterpek, L.*, et al.* Peripheral myelin protein 22 is a constituent of intercellular junctions in epithelia. *Proc Natl Acad Sci U S A* **98**, 14404-14409 (2001).
10. Roux, K.J., Amici, S.A. & Notterpek, L. The temporospatial expression of peripheral myelin protein 22 at the developing blood-nerve and blood-brain barriers. *J Comp Neurol* **474**, 578-588 (2004).
11. Roux, K.J., Amici, S.A., Fletcher, B.S. & Notterpek, L. Modulation of epithelial morphology, monolayer permeability, and cell migration by growth arrest specific 3/peripheral myelin protein 22. *Mol Biol Cell* **16**, 1142-1151 (2005).
12. Neuberg, D.H., Sancho, S. & Suter, U. Altered molecular architecture of peripheral nerves in mice lacking the peripheral myelin protein 22 or connexin32. *J Neurosci Res* **58**, 612-623 (1999).

13. Guo, J.*, et al.* Abnormal junctions and permeability of myelin in PMP22-deficient nerves. *Ann Neurol* **75**, 255-265 (2014).

14. Young, P.*, et al.* E-cadherin is required for the correct formation of autotypic adherens junctions of the outer mesaxon but not for the integrity of myelinated fibers of peripheral nerves. *Mol Cell Neurosci* **21**, 341-351 (2002).

15. Verhamme, C.*, et al.* Myelin and axon pathology in a long-term study of PMP22-overexpressing mice. *J Neuropathol Exp Neurol* **70**, 386-398 (2011).

16. Adlkofer, K.*, et al.* Hypermyelination and demyelinating peripheral neuropathy in Pmp22-deficient mice. *Nat Genet* **11**, 274-280 (1995).

17. Schindelin, J.*, et al.* Fiji: an open-source platform for biological-image analysis. *Nat Methods* **9**, 676-682 (2012).

18. Kourtidis, A., Ngok, S.P. & Anastasiadis, P.Z. p120 catenin: an essential regulator of cadherin stability, adhesion-induced signaling, and cancer progression. *Prog Mol Biol Transl Sci* **116**, 409-432 (2013).

19. Campas, O., Noordstra, I. & Yap, A.S. Adherens junctions as molecular regulators of emergent tissue mechanics. *Nat Rev Mol Cell Biol* **25**, 252-269 (2024).

20. Hu, B.*, et al.* Tuning PAK Activity to Rescue Abnormal Myelin Permeability in HNPP. *PLoS Genet* **12**, e1006290 (2016).

21. Altevogt, B.M., Kleopa, K.A., Postma, F.R., Scherer, S.S. & Paul, D.L. Connexin29 is uniquely distributed within myelinating glial cells of the central and peripheral nervous systems. *J Neurosci* **22**, 6458-6470 (2002).

22. Paivalainen, S. & Heape, A.M. Myelin-associated glycoprotein and galactosylcerebroside expression in Schwann cells during myelination. *Mol Cell Neurosci* **35**, 436-446 (2007).

23. Rash, J.E.*, et al.* KV1 channels identified in rodent myelinated axons, linked to Cx29 in innermost myelin: support for electrically active myelin in mammalian saltatory conduction. *J Neurophysiol* **115**, 1836-1859 (2016).

24. Cai, Z.*, et al.* Tomacula in MAG-deficient mice. *J Peripher Nerv Syst* **7**, 181-189 (2002).

25. Rasband, M.N. & Peles, E. Mechanisms of node of Ranvier assembly. *Nat Rev Neurosci* **22**, 7-20 (2021).

26. Tricaud, N., Perrin-Tricaud, C., Bruses, J.L. & Rutishauser, U. Adherens junctions in myelinating Schwann cells stabilize Schmidt-Lanterman incisures via recruitment of p120 catenin to E-cadherin. *J Neurosci* **25**, 3259-3269 (2005).

Acknowledgements

This work was supported by an NIH K22 Award (K22NS125057) and a Johns Hopkins Merkin Peripheral Neuropathy and Nerve Regeneration Center Grant to Kathryn Moss. This research was also supported by the Johns Hopkins Microscope Facility (Office of the Director and the National Institute of General Medical Sciences of the National Institutes of Health award number S10OD023548) and the Johns Hopkins Neuroscience Imaging Center.

Declaration of Interests

The authors have declared no competing interests.

Materials and Methods

Animal Husbandry

All experiments were conducted with approval from the Johns Hopkins Animal Care and Use Committee. C3-PMP mice (B6.Cg-Tg(PMP22) C3Fbas/J, referred to as CMT1A mice) were obtained from the Jackson Laboratory (Stock #: 030052), maintained/expanded as heterozygotes by breeding with C57BL/6J wildtype mice (The Jackson Laboratory, Stock #: 000664) and genotyped according to the suggested protocol. LacZ PMP22 Deficient mice (referred to as HNPP mice) were obtained from Regeneron via Dr. Lucia Notterpek, maintained/expanded as heterozygotes by breeding with 129S1/SvImJ wildtype mice (The Jackson Laboratory, Stock #: 002448) and genotyped according to the suggested protocol[16]. A balanced representation of male and female mice aged 3 months were perfused and their sciatic nerves were harvested to prepare teased nerve fibers for immunostaining.

Perfusion and Teased Nerve Fibers

Mice were anesthetized with Isoflurane and transcardiac perfusion was performed under anesthesia. The blood was cleared with PBS perfusion followed by perfusion with 4% paraformaldehyde prepared in PBS. After perfusing, both sciatic nerves were removed and post-fixed in 4% paraformaldehyde for three hours at 4° C. The nerves were then washed five times quickly with cold PBS and stored at 4° C overnight. The next day the tibial branch was isolated in a dish of cold PBS and cut into four segments. Each segment was transferred to a drop of PBS on a Superfrost Plus microscope slide (Fisher Scientific) and gently teased to separate the nerve fibers. After teasing, excess PBS was removed and the teased nerve fiber slides were dried at room temperature overnight. The slides were stored at -80° C the next day until ready for immunofluorescence staining.

Immunofluorescence Staining of Teased Nerve Fibers

Teased nerve fibers for immunofluorescence were permeabilized by submerging the slides in -20° C chilled Acetone in Coplin jars for ten minutes while rocking at room temperature. After removing the acetone, the fibers were washed in PBS three times for five minutes each while rocking at room temperature. The edges of

each slide were quickly dried and a boundary around the fibers was drawn using a PAP pen. This was performed one slide at a time to prevent drying of the nerve fibers. Slides were resubmerged in the last PBS wash after the PAP boundary was dry. Excess PBS was removed from each slide before placing the slides into an immunostaining tray and adding 0.5ml of antibody buffer to each (190ml - PBS, 10ml - 40-50% Fish Gelatin [Sigma Aldrich, G7765] and 200ul Triton X-100, 10ml aliquots stored at -20° C). This was performed in batches of three slides to prevent drying of the nerve fibers. The nerve fibers were blocked with antibody buffer at room temperature for one hour. Primary antibody solutions (see table for concentrations) were prepared in antibody buffer on ice. After removing the antibody buffer used for blocking, 0.5ml of primary antibody solution was added to each slide and incubated at 4° C overnight.

Primary Antibody	Company, Cat. Number	Species	Concentration
anti-ZO-1	DSHB, R26.4C	Rat	1:50
anti-E-Cadherin	Thermo Fisher, 14-3249-82	Rat	1:100
anti-β-Catenin	Sigma-Aldrich, C2206	Rabbit	1:500
anti-p120-Catenin	Thermo Fisher, PA5-82545	Rabbit	1:500
anti-Connexin29	Thermo Fisher, 34-4200	Rabbit	1:50
anti-Kv1.2	Absolute Antibody, Ab02104-23.0	Rabbit	1:500
anti-Nav (Pan)	Absolute Antibody, Ab02113-8.1	Rat	1:500
anti-Neurofascin155	R&D Systems, AF3235	Chicken	1:500
anti-Caspr1	Abcam, ab34151	Rabbit	1:1000

The nerve fibers were washed in PBS three times for ten minutes each while rocking at room temperature. Primary antibody solutions (see table for concentrations) were prepared in antibody buffer on ice. Excess PBS was removed from each slide before placing the slides into an immunostaining tray and adding 0.5ml of secondary antibody solution to each. This was performed in batches of three slides to prevent drying of the nerve fibers. The nerve fibers were incubated with secondary antibody at room temperature for one and a half hours.

Secondary Antibody	Company	Concentration
MAG Alexa Fluor 488	Sigma-Aldrich, MAB1567A4	1:100
405 Phalloidin	Thermo Fisher, A30104	1:400
Goat anti-Rabbit Alexa Flour 488	Thermo Fisher, A11034	1:1000
Goat anti-Rat Alexa Fluor 568	Thermo Fisher, A11077	1:1000
Goat anti-Chicken Alex Fluor 647	Thermo Fisher, A11041	1:1000

The nerve fibers were washed in PBS three times for ten minutes each while rocking at room temperature. Excess PBS was removed, 60µl Prolong Gold antifade reagent (Thermo Fisher, P36930) was added to each and topped with No. 1.5H Precision cover glass. Slides were dried at room temperature overnight in the dark and stored at -20° C the next day until ready for imaging.

Confocal and Widefield Immunofluorescence Imaging, Data Analysis and Statistics

Confocal imaging was performed using a Zeiss LSM800 or Zeiss LSM880. Z-stacks were acquired from at least six different regions of the slide and analyzed using Imaris x64 version 9.2.1 (Oxford Instruments, Bitplane). Five SLIs from at least three different nerve fibers were manually outlined in each image to create isosurfaces. Mean signal intensity was measured within each isosurface as a readout of SLI mean signal intensity. The signal for a channel of interest was then duplicated only within each SLI isosurface and a threshold was established as real signal for each antibody. A second isosurface was created within each SLI isosurface by setting the established threshold for each antibody. The volume of the second isosurface was recorded and the diameter of the nerve fiber at each SLI (axon + myelin sheath) was recorded. The distribution at SLIs was calculated by normalizing each thresholded volume to the fiber diameter for that SLI. Widefield fluorescence imaging of β-Catenin and F-Actin was also performed using a Zeiss Axio Imager Z1 with a 40X oil objective. Tiled z-stacks were acquired from at least four large regions and analyzed using Fiji[17]. The distance between SLIs was manually traced using the freehand tool for fibers in which at least 5 consecutive SLIs were visible. The distance between SLIs was averaged for each individual nerve fiber and these measures were averaged as a readout of the distance between SLIs.

All data were evaluated for significance by unpaired t-test using Prism 9 (GraphPad). For each experiment, the data were analyzed by unpaired t-test on all individual SLIs and the average from each biological replicate. Significance detected ($p < 0.05$) using the average from each biological replicate was considered significant whereas significance detected ($p < 0.05$) using data from each individual SLI was considered biological insignificant but was used as a readout of potential significance for incomplete datasets. The statistical test used, exact n, definition of what n represents and the definition of center and dispersion for

each analysis is located in the figure legends. Randomization was performed for all experiments by randomly selecting mice from multiple litters. No data points from any assay were excluded from this study.